Australian Earthquake Engineering Society
2022 National Conference, 24-25 November 2022
Mount Macedon, Victoria, Australia

Stochastic Finite-fault Ground Motion Simulation of the 2021 M_W5.9 Woods Point Earthquake: Methodology and Preliminary Results

Yuxiang Tang[1], P. Martin Mai[1]

1. PSE Division, King Abdullah University of Science and Technology, 23955 Thuwal Saudi Arabia.

Correspond to: yuxiang.tang@kaust.edu.sa

Abstract

To better understand the physics of the 2021 M_w 5.9 Woods Point earthquake that occurred in Victoria state, Australia, we apply a stochastic finite-fault approach to simulate ground motions for 36 selected sites. We determine the input parameter values for regional geometric spreading and anelastic attenuation, path duration, site amplification, and Kappa value, from regression analysis of the observed Fourier Amplitude Spectra (FAS). We then determine the dynamic stress drop value by minimizing the residuals between the simulated and observed 5%-damped pseudo-spectral acceleration (PSA). We investigate the capability of the proposed stochastic model by comparing the simulated ground motions with the observations. Finally, we compare the simulated 5%-damped PSA with six GMMs selected for the NSHA (National Seismic Hazard Assessment) program, revealing that our simulations are within the acceptance range defined by the GMMs.

Keywords: Woods Point earthquake; stochastic simulation; attenuation model; GMSS2.0.

1 Introduction

Ground motion simulation is an important approach to generating synthetic time series of earthquake shaking for scientific and engineering purposes, such as facilitating regional seismic hazard analysis (Boore, 1983; Atkinson and Boore, 1995, 2006; Edwards and Fäh, 2013). According to Douglas (2022), over 600 ground motion models (GMMs), an important tool for ground motion characterisation in probabilistic seismic hazard analysis (PSHA), have been developed during the past 50 years (1970-2020) internationally, and ~90 of the GMMs are developed by simulation-based approaches. Stochastic simulation plays a particularly significant role in estimating ground shaking levels (especially for high-frequency ground motions) for low-to-moderate seismicity regions where strong ground motion observations are often scarce (Lam et al., 2000; Allen et al., 2007; Tang et al., 2020). For regions with abundant observational data, stochastic simulations are widely used in hybrid ground motion calculation to estimate high-frequency shaking (Pezeshk et al., 2018; Jayalakshmi et al., 2021).

By combining band-limit Gaussian white noise with a deterministic seismological model, Boore (1983; 2003) proposed an approach to generate synthetic accelerograms in which the seismological model is used as a filter in the Fourier domain defining the amplitude spectrum

that is composed of source, path, and site components. Based on the source model, two categories of stochastic ground motion simulation can be defined, the point-source model (Brune, 1970; Boore, 2003) and the finite-fault source model (Beresnev and Atkinson, 1998a, b; Motazedian and Atkinson, 2005). These two general approaches are encoded in two widely used software packages, SMSIM and EXSIM, respectively (Boore, 2003; Motazedian and Atkinson, 2005). Compared to SMSIM (point source), EXSIM (finite-fault source) is advantageous in considering the geometric properties and directivity effects of earthquake source in the simulation process, thus allowing to estimate ground motion amplitudes for large earthquakes at close distances from the causative fault, with a higher level of accuracy (Atkinson and Assatourians, 2015).

In this study, we use the recently developed GMSS (Ground Motion Simulation System) codes. Both GMSS1.0 (1D point source) and GMSS2.0 (2D finite-fault source) have been verified and validated against SMSIM and EXSIM, real earthquake observations, as well as GMMs (Tang et al. 2021; Tang 2022a, b).

As the largest earthquake that occurred in Victoria's recorded history, the 2021 M_w5.9 earthquake has drawn the attention of seismologists, engineers, and other communities (e.g., Hoult et al., 2021; Sinadinovski et al., 2021; Love, 2021). Even though the relatively large amount of well-recorded data allows us to investigate ground motion properties in detail, simulation-based data that encode earthquake physics with well-calibrated parameters are needed to facilitate local seismic hazard/ risk analysis. Therefore, we simulate ground motions for this event (using the GMSS2.0 code) to analyse regional ground motion shaking levels that are important for seismic hazard analysis.

2 Methodology

2.1 Stochastic finite-fault modelling

As stated in previous studies (e.g., Beresnev and Atkinson, 1997; Motazedian and Atkinson, 2005; Boore, 2009), the basic principle of finite-fault modelling is to divide the fault source into several subfaults, where each subfault is regarded as a point source. Each point source radiates an elementary seismic wave. The final time series of ground motion is then obtained by summation of the time series generated by all subfaults, with a proper time delay between subfaults to parameterise the rupture evolution over the fault plane (Fig .1).

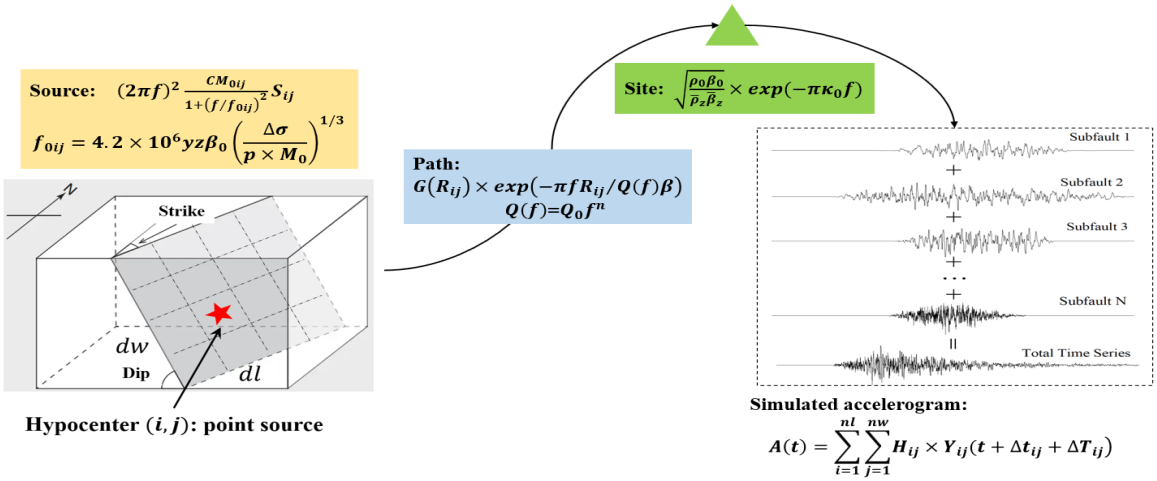

Figure 1. Illustration of finite-fault modelling. A detailed description is provided in the main text.

The Fourier amplitude spectrum (FAS) of acceleration of a point source is given by Eq. (1):

$$FAS_{ij} = E_{ij} \times G_{ij} \times Ae_{ij} \times Am \times An \quad (1)$$

where FAS_{ij} is FAS of acceleration of the ij^{th} subfault; E_{ij} is the earthquake source model; G_{ij} represents geometric spreading at distance R_{ij}; Ae_{ij} indicates the whole path anelastic attenuation; Am and An are the local site amplification and diminishing factor, respectively.

The earthquake source is expressed by Eq. (2):

$$E_{ij} = (2\pi f)^2 \frac{CM_{0ij}}{1+(f/f_{0ij})^2} S_{ij} \quad (2)$$

where, C is a scaling factor, given as $C = 0.55 \times 2.0 \times 0.707)/4\pi\rho_0\beta_0^3$, whereby ρ_0 and β_0 are density and S-wave velocity at the source; M_{0ij}, f_{0ij} and S_{ij} are seismic moment, corner frequency, and scaling factor for the ij^{th} subfault, respectively.

M_{0ij} can be determined using Eq. (3):

$$M_{0ij} = \frac{M_0 W_{ij}}{\sum_{l=1}^{nl}\sum_{w=1}^{nw} W_{lw}} \quad (3)$$

where M_0 is the total seismic moment and W_{ij} is the relative slip weight of the ij^{th} subfault; nl and nw are the number of subfaults along strike and down dip of the finite fault, respectively.

f_{0ij} is defined by Eq. (4) (Tang, 2022a):

$$f_{0ij} = 4.9 \times 10^6 \beta_0 \left(\frac{\Delta\sigma}{p \times M_0}\right)^{1/3} \quad (4a)$$

$$f_{0ij} = 4.2 \times 10^6 yz\beta_0 \left(\frac{\Delta\sigma}{p \times M_0}\right)^{1/3} \quad (4b)$$

in which, $\Delta\sigma$ is dynamic stress drop, y is the ratio between rupture velocity and shear-wave velocity, and z defines the strength of high-frequency radiation and correlates with the slip fraction.

In Eq. (4), p is the parameter defining the pulsing percentage, determined by Eq. (5):

$$p = \begin{cases} N_R/N, & N_R < N \times pp \\ pp, & N_R \geq N \times pp \end{cases} \quad (5)$$

where N_R is the cumulative number of pulsing subfaults, and it is determined by the rupture area percentage (pp); N is the total number of subfaults.

S_{ij} in Eq. (2), is the scaling factor introduced by Boore (2009), which is used to eliminate the influences of subfault size on spectral amplitude at lower frequencies due to the incoherent summation. S_{ij} is calculated by Eq. (6):

$$S_{ij} = CS_{ij} \frac{1+(f/f_{0ij})^2}{1+(f/f_{0effij})^2} \quad (6a)$$

where

$$CS_{ij} = \sqrt{N}/H_{ij} \quad (6b)$$

$$f_{0effij} = f_{0ij}/\sqrt{CS_{ij}} \quad (6c)$$

H_{ij} in Eq. (6b) is the high-frequency scaling factor. The acceleration-based H_{ij} is expressed by Eq. (7a), which can be simplified as Eq. (7b) (Boore, 2009):

$$H_{ij} = (M_0/M_{0ij}) \times \sqrt{\sum\left(\frac{f_0^2 f}{f_0^2+f^2}\right)^2 \Big/ N \sum\left(\frac{f_{0ij}^2 f}{f_{0ij}^2+f^2}\right)^2} \quad (7a)$$

$$H_{ij} = \sqrt{N}\left(\frac{f_0}{f_{0ij}}\right)^2 \quad (7b)$$

Here, f_0 is the overall corner frequency for the rupture, determined from Eq. (8) (Tang, 2022a):

$$f_0 = 4.9 \times 10^6 \beta_0 \left(\frac{\Delta\sigma}{M_0}\right)^{1/3} \quad (8a)$$

$$f_0 = 4.2 \times 10^6 yz\beta_0 \left(\frac{\Delta\sigma}{M_0}\right)^{1/3} \quad (8b)$$

The geometrical spreading G_{ij} in Eq. (1) relates to subfault distance R_{ij} from the received, and accounts for the regional geometric attenuation of seismic-wave amplitudes along the wave-propagation path.

Ae_{ij} in Eq. (1) is expressed by Eq. (9):

$$Ae_{ij} = \exp\left(\frac{-\pi f R_{ij}}{Q\beta_0}\right) \quad (9)$$

where Q is the regional quality factor which is inversely related to anelastic attenuation.

Am and An in Eq. (1) can be calculated by Eq. (10) and (11), respectively:

$$Am = \sqrt{\frac{\rho_0\beta_0}{\bar{\rho}_z\bar{\beta}_z}} \quad (10)$$

where $\bar{\rho}_z$ and $\bar{\beta}_z$ are the time-averaged density and shear-wave velocity over the depth corresponding to a quarter wavelength.

$$An = exp\left(-\pi\kappa_0 f\right) \quad (11)$$

where κ_0 represents the spectral decay slope at high frequencies.

The final time series of the finite-fault source can then be computed using Eq. (12):

$$A(t) = \sum_{i=1}^{nl}\sum_{j=1}^{nw} H_{ij} \times Y_{ij}(t + \Delta t_{ij} + \Delta T_{ij}) \quad (12)$$

where $A(t)$ is the total time series of the seismic signal at a site; $Y_{ij}(t)$ is the signal of the ij^{th} subfault, obtained from the inverse Fourier transform of FAS_{ij} (Eq. 1); Δt_{ij} is the delay time of the ij^{th} subfault along the path; and ΔT_{ij} is the delay time for ij^{th} subsource and is proportional to the rise time of the subfault (T_{0ij}).

2.2 The GMSS code

We use the code package GMSS2.0 that builds on EXSIM_DMB (Boore, 2009) and EXSIM_V3 (Crane and Motazedian, 2014) and thus is an enhanced software package for stochastic finite-fault ground motion simulation. Particularly, GMSS2.0 has the following features:

- Every step is transparent, enabling users to check every single module and function, and make changes based on specific requirements.
- Two different options are included for calculating corner frequency and rise time, namely rupture-velocity dependent and independent models, thus improving ground motion estimation at high frequencies.
- Rupture dimensions are estimated using empirical relationships (Table 1).
- Site-specific simulations with various site responses for different sites are possible as alternative options.
- Computationally efficient with the application of parallel computing toolbox in MATLAB.

The workflow chart of the GMSS2.0 code/algorithm is shown in Fig. 2.

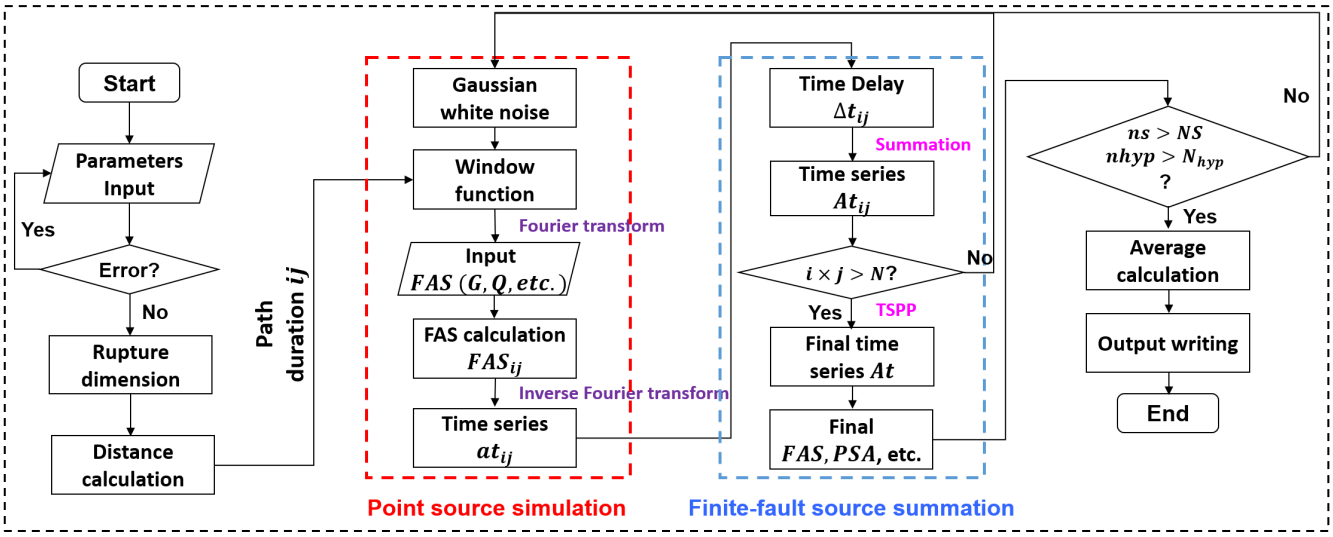

Figure 2. Workflow chart of GMSS2.0 code.

Generally, users need to provide three types of input in the "Parameters Input" module, namely, (i) the general input parameters, such as the time interval (dt), number of simulations per hypocenter (NS), and number of hypocenters (N_{hyp}); (ii) source parameters, such as strike and dip angle of the fault, stress drop ($\Delta\sigma$), corner-frequency indicator, etc; and (iii) site parameters, including the location of sites (longitude and latitude, or distance and azimuth), site condition (V_{S30} and κ_0), etc. For determining the rupture, GMSS2.0 provides four published source-scaling relationships (Table 1), including ones developed for the stable continental region, subduction interface region, and China mainland region.

Table 1. Rupture scaling relationship embodied in GMSS2.0.

Relationship	WC94	L10	T17	C19
Reference	Wells and Coppersmith (1994)	Leonard (2010)	Thingbaijam et al. (2017)	Cheng et al. (2019)
Normal	$FL = 10^{-1.88+0.50M}$ $FW = 10^{-1.14+0.35M}$	$FL = 10^{-2.54+0.60M}$ $FW = 10^{-1.46+0.40M}$	$FL = 10^{-1.722+0.485M}$ $FW = 10^{-0.829+0.323M}$	$FL = 10^{-4.02+0.83M}$ $FW = 10^{-2.13+0.51M}$
Reverse	$FL = 10^{-2.42+0.58M}$ $FW = 10^{-1.61+0.41M}$	$FL = 10^{-2.54+0.60M}$ $FW = 10^{-1.46+0.40M}$	$FL = 10^{-2.693+0.614M}$ $FW = 10^{-1.669+0.435M}$	$FL = 10^{-3.27+0.72M}$ $FW = 10^{-1.67+0.44M}$
Strike-slip	$FL = 10^{-2.57+0.62M}$ $FW = 10^{-0.76+0.27M}$	$FL = 10^{-2.50+0.60M}$ $FW = 10^{-1.49+0.40M}$	$FL = 10^{-2.943+0.681M}$ $FW = 10^{-0.543+0.261M}$	$FL = 10^{-2.45+0.61M}$ $FW = 10^{-1.38+0.41M}$
Undefined	$FL = 10^{-2.44+0.59M}$ $FW = 10^{-1.01+0.32M}$	$^{*}FL = 10^{-2.59+0.60M}$ $^{*}FW = 10^{-1.60+0.40M}$	$^{\dagger}FL = 10^{-2.412+0.583M}$ $^{\dagger}FW = 10^{-0.88+0.366M}$	$FL = 10^{-2.67+0.63M}$ $FW = 10^{-1.38+0.40M}$
(Note: FL and FW are the fault length and width respectively; M is the moment magnitude; FW in L10 is obtained using the correlation between fault area and FL, assuming the fault is rectangular; FW in Cea19 is obtained using the correlation between FL and FW. The unit for FL and FW is km in this study; "*" means this scaling relationship is specifically for Stable Continental Region; "†" means this scaling relationship is specifically for Subduction Interface)				

Considering the variations in engineering demands, GMSS2.0 computes seven different distances in the distance matrices, including R_{rup} (closet distance to fault rupture) and R_{jb} (closet distance to the surface projection of fault rupture). The procedures in the box marked red in Fig.3 are the simulation procedures for a single subfault, following stochastic point-source simulation procedures (Boore, 2003; Tang, et al. 2021). The procedures in the blue box define the additional steps for finite-fault simulations in which the time series of each subfault are summed with proper time delays. The final simulation outputs provided by GMSS2.0

include the time series of one or several random simulations, averaged intensities (i.e., PGA, PGV, PGD, I_A (Arias intensity), CAV (Cumulative Absolute Velocity), PSA and duration), averaged FAS, Husid plot, and more. Further information can be found in Tang (2022b). The user manual and source code are available at https://github.com/Y-Tang99/GMSS2.0.

3 Simulation of the 2021 M_w5.9 Woods Point Earthquake

For better ground motion characterisation (GMC) and seismic hazard assessment purposes, we perform stochastic finite-fault simulations of ground motions recorded by 36 stations using the GMSS2.0 code. The raw data have been processed as follows:

- Bandpass filter seismic records, using a 4th order acausal Butterworth filter with a frequency range of 0.05 Hz and variable high-frequency cut-off that varies due to station-dependent instrument sampling rate.
- Remove instrument response using station *XML* files generated by Obspy (https://docs.obspy.org/tutorial/code_snippets/stationxml_file_from_scratch.html).
- Determine signal-to-noise ratio (SNR) for each station at 20 frequencies of interest for all 3 components; discard observations with low SNR (i.e., SNR < 5.0).
- Smooth the FAS using the window proposed by Katsuaki and Ohmachi (1998).

We determine the parameter values for simulations by regression analysis of FAS at 20 discrete frequencies ranging from 0.1 Hz to 20 Hz. The site amplification model follows Seyhan and Stewart (2014), but the linear term (V_{S30}-scaling) coefficient is modified from the local V_{S30} values of the 36 stations, while the nonlinear term is computed using the local PGA values on the reference rock site with V_{S30} = 760 m/s. Geometric spreading and anelastic attenuation are determined using the functional format proposed by Boore et al. (2009), where we adopt a bi-linear geometric spreading, and a bilinear Q factor (when plotted in log-log format). The source duration is determined as $0.27/f_0$ (Tang, 2022a) while the path duration was determined following Boore and Thompson (2014). The source parameters, including the seismic moment and corner frequency, are determined by matching the theoretical Brune model of the Fourier displacement spectrum (Brune, 1970) with the reference spectrum obtained from the regression. Finally, the dynamic stress drop value is determined by minimizing the absolute residual value of 5%-damped PSA between observations and simulations over all distance and frequency ranges.

The geographical locations of stations selected for this study are shown in Fig. 3. Simulation results are displayed in Fig. 4, and the corresponding residuals are given in Fig. 5. Comparisons of 5%-damped PSA with six GMMs (listed in Table 2) are shown in Fig. 6.

The simulations in Fig. 4 are site-specific with various V_{S30} values, indicating that the simulated PSA's generally match the observations for the hypocentral distance range 67.6 km (CLIF station) to 439.1 km (AUUHS) and for spectral periods ranging from 0.05 s to 3.0 s (note that station CNB, only the range 0.08 s to 3.0 s was usable due to low sampling rate). The mean residual between simulations and observations over all distances over the spectral periods of interest is shown in Fig. 5. The average residual is very close to 0, indicating that the input parameters have been well calibrated for this event based on the available data.

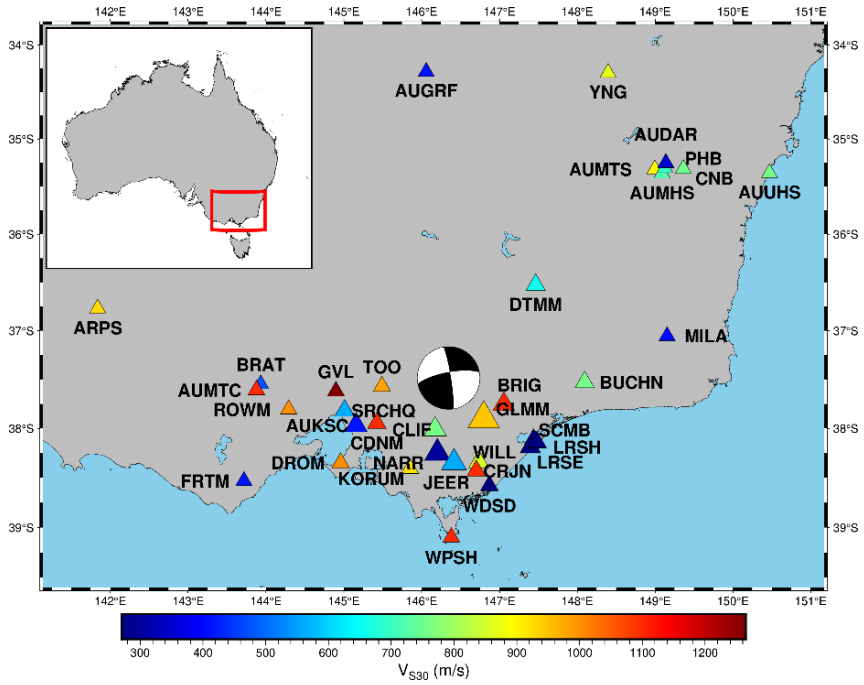

Figure 3. Selected stations in this study (different size of the symbol indicates the PGA value recorded by the station).

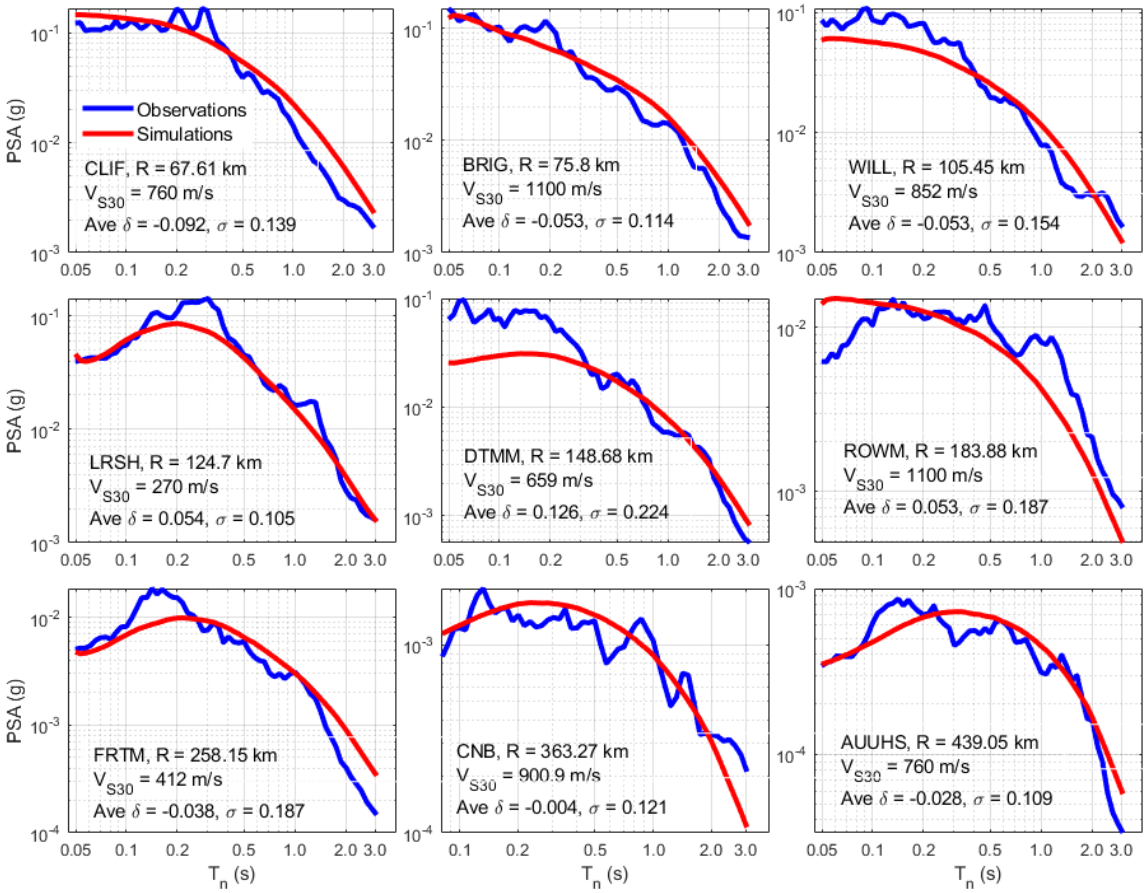

Figure 4. Comparison of simulated 5%-damped pseudo-spectral acceleration (PSA) and observations for nine stations. Observations are given as the geometric mean of the two horizontal components.

(a) (b)

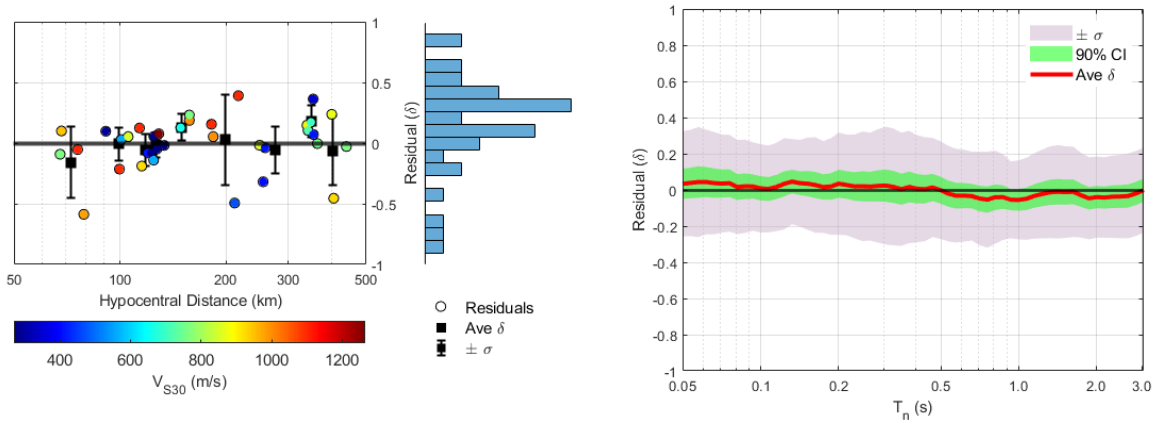

Figure 5. Overall residuals between simulations and observations of 5%-damped PSA, (a) Residuals with respect to distance (the black square indicates the average residual over various distance bins; the corresponding central distances for each bin are 72.63, 99.19, 117.83, 126.31, 149.20, 198.44, 275.34, 349.30 and 401.35 km; σ indicates the standard deviation of each distance bin); (b) Residuals with respect to natural periods between 0.05 – 3.0 s, the green shaded area marks the 90% confidence interval. δ indicates the average residual, and σ represents the standard deviation. Observations are given as the geometric mean of the two horizontal components.

In terms of ground-motion models (GMM), the AB06 model is a typical GMM developed for Central Eastern North America (CENA) but also applied in other stable continental regions (Atkinson and Boore, 2006). The Sea09 model is simulation-based, and we only consider the non-cratonic condition in this study (Somerville, et al., 2009). The A12 model is a GMM specifically developed for South-eastern Australia (SEA) (Allen 2012). The Bea14 model is an NGA-West2 model which is mainly for active tectonic regions (Boore et al., 2014). The Gea18 model is a comprehensive averaged GMM that considers 17 different models with different weights at different spectral periods and is typically applied in stable continental regions (Goulet et al. 2018). The Tea20 model is a regionally adjustable GMM developed for intraplate events (Tang et al., 2020). All GMMs are adjusted to the average site condition V_{S30} = 725.1 m/s.

Table 2. Selected GMMs in this study

No.	GMM	Region	Type	Distance	Reference V_{S30} (m/s)	Reference
1	AB06	CENA	Semi-simulated (Finite-fault source)	R_{rup}	760	Atkinson and Boore (2006)
2	Sea09	Australia	Simulated (broadband)	R_{JB}	865	Somerville et al. (2009)
3	A12	SEA	Semi-simulated (Finite-fault source)	R_{rup}	820	Allen (2012)
4	Bea14	Crustal active	Empirical	R_{JB}	760	Boore et al. (2014)
5	Gea18	CENA	Combined	R_{rup}	3000	Goulet et al. (2018)
6	Tea20	Regionally adjustable	Semi-simulated (Point source)	R_{eff}	760	Tang et al. (2019, 2020)

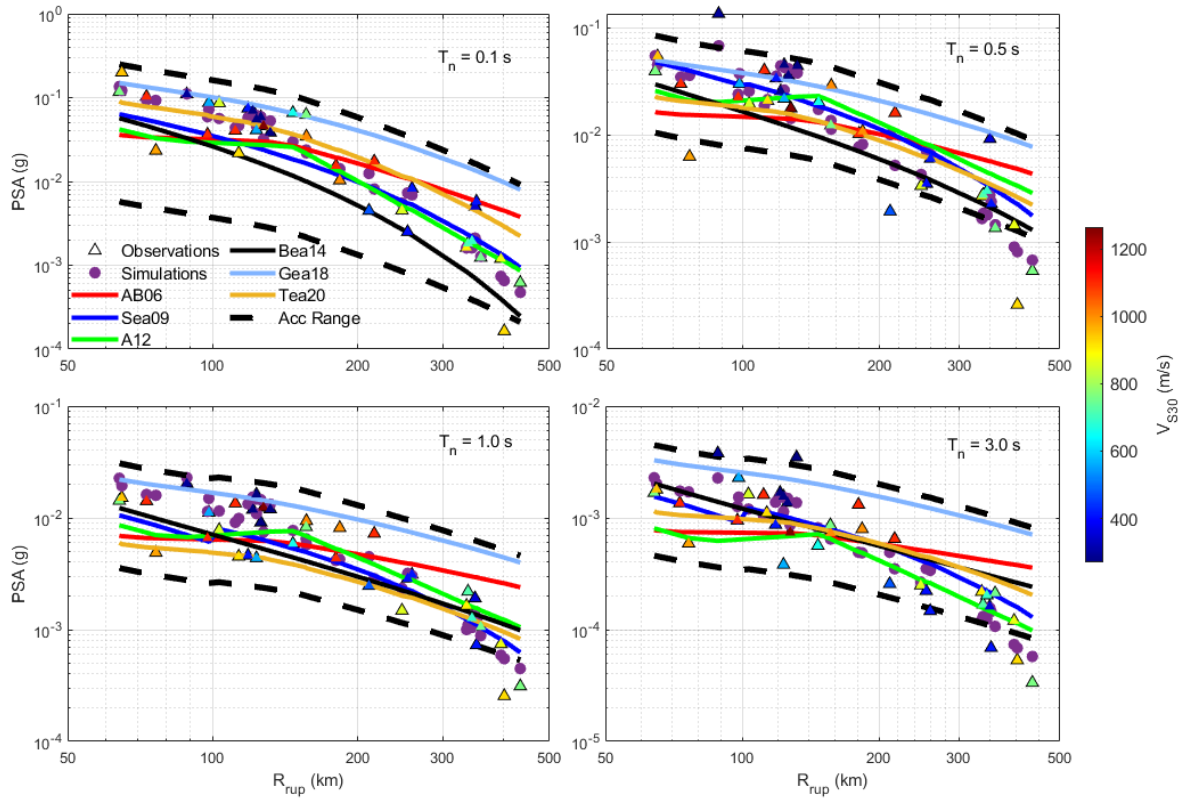

Figure 6. Comparison of 5%-damped pseudo-spectral acceleration (PSA) and six GMMs at four spectral periods. The bound between dashed lines indicates the acceptance range defined by the GMMs (Goulet et al., 2015). The GMMs have been adjusted to the average site with V_{S30} = 725.1 m/s.

Next., we discuss the comparisons between GMM-predictions and our simulations for 5%-damped PSA for four spectral periods (Fig. 6). We find that the simulated PSA values generally match the observations and lie within the acceptance range of the selected GMMs. The acceptance range is defined as the range between the upper and lower bounds of the selected GMMs. The largest GMM prediction from all models at any period is selected as a reference point, to which 15% is added (this number is selected based on judgment to increase the allowable range, pp. 25 in Goulet et al. (2015)). The upper-bound spectrum is then defined by applying the ratio of the reference point to the average spectrum. The lower-bound spectrum is obtained from the same process (Goulet et al., 2015). This indicates our simulation results are acceptable. Generally, the performance of the GMMs is better at shorter periods and closer distances. As observed by Hoult et al. (2021), the local GMMs (Sea09, A12, and Tea20) perform better and generally reflect the ground motion attenuation characteristics of this event. The AB06 model appears to underestimate ground motions for distances less than 150 km and overestimates at distances above 150 km. In contrast, the Gea18 model overestimates ground motions for the entire distance range considered in the study.

Our result may be a reference to inspecting the overall performance of the CENA models for predicting the Australian ground motions. Because there are no recordings at short distances for this event, it is currently impossible to judge their performance at close distances, even though Allen and Atkinson (2007) found that the attenuation properties between SEA and CENA are similar at short distances. The Bea14 model (for active tectonic regions) leads to underestimates at short periods, which is also shown in Hoult et al. (2021).

4 Closing Remarks

This study analyses synthetic and observed ground motions of the 2021 M_w5.9 Woods Point earthquake, using the recently introduced ground-motion simulation code GMSS2.0. This software package implements stochastic finite-fault ground motions in low-to-moderate seismicity regions where instrument observations are scarce. We describe the basic principles and features of GMSS2.0 and then apply the code to simulate the ground motions of the 2021 M_w5.9 Woods Point earthquake. We achieve good agreement between simulations and field observations, with the input parameters determined from 36 selected stations. We also compared our simulations with six GMMs considered in the NSHA program; the results show that the simulated ground motions are within the acceptance range defined by the GMMs.

In a follow-up study, we will generate a large simulation-based dataset at a wide distance range with varying source, path, and site parameters to conduct a detailed sensitivity analysis. The corresponding results will facilitate future work on regional PSHA in the context of ground motion characterisation over a wide distance range in the absence of observational data.

5 Acknowledgment

We thank Trevor Allen from Geoscience Australia, Adam Pascale from Seismology Research Center in Australia, and Ryan Hoult from Université Catholique de Louvain in Belgium for providing the recording data. We thank Januka Attanayake and Abraham Jones from The University of Melbourne for their help in removing the instrument response from the raw data. We thank David Love from the Seismological Association of Australia Inc. and Wayne Peck from Seismology Research Center for their help in determining the source mechanism. We thank David Boore for his insightful comments on determining the parameter values used in the simulations. We also thank Laura Parisi and Bo Li from Computational Earthquake Seismology (CES) group at King Abdullah University of Science and Technology (KAUST) in Thuwal, Saudi Arabia for their general help in preparing this manuscript. The research presented in this article is supported by King Abdullah University of Science and Technology (KAUST) in Thuwal, Saudi Arabia, Grant BAS/1/1339-01-01.

6 References

Allen, T. (2012). Stochastic ground-motion prediction equations for southeastern Australian earthquakes using updated source and attenuation parameters, Geoscience Australia, Canberra, Record 2012/69.

Allen, T., Cummins, P., Dhu, T. and Schneider, J. (2007). Attenuation of Ground-Motion Spectral Amplitudes in Southeastern Australia, Bull Seismol Soc Am, Vol 97, No 4, pp 1279-1292.

Allen, T. I. and Atkinson, G. M. (2007). Comparison of Earthquake Source Spectra and Attenuation in Eastern North America and Southeastern Australia, Bull Seismol Soc Am, Vol 97, No 4, pp 1350–1354.

Atkinson, G. M. and Assatourians, K. (2015). Implementation and Validation of EXSIM (A Stochastic Finite-Fault Ground-Motion Simulation Algorithm) on the SCEC Broadband Platform, Seismol Res Letts, Vol 86, No 1, pp 48-60.

Atkinson, G. M., and Boore, D. M. (1995). Ground motion relations for eastern North America, Bull Seismol Soc Am, Vol 85, pp 17-30.

Atkinson, G. M., and Boore, D. M. (2006). Earthquake Ground-Motion Prediction Equations for Eastern North America, Bull Seismol Soc Am, Vol 96, No 6, pp 2181-2205.

Beresnev, I. A., and Atkinson, G. M. (1997). Modeling finite fault radiation from the ω^n spectrum, Bull Seismol Soc Am, Vol 87, pp 67-84.

Beresnev, I. A., and Atkinson, G. M. (1998a). Stochastic Finite-Fault Modeling of Ground Motions from the 1994 Northridge, California, Earthquake, I. Validation on Rock Sites, Bull Seismol Soc Am, Vol 88, No 6, pp 1392-1401.

Beresnev, I. A., and Atkinson, G. M. (1998b). FINSIM-a FORTRAN Program for Simulating Stochastic Acceleration Time Histories from Finite Faults, Seismol Res Letts, Vol 69, No 1, pp 27-32.

Boore, D. M. (1983) Stochastic simulation of high-frequency ground motions based on seismological models of the radiated spectra, Bull Seismol Soc Am, Vol 73, pp 1865–1894.

Boore, D. M. (2003). Simulation of Ground Motion Using the Stochastic Method, Pure Appl Geophys, Vol 160, pp 635-676.

Boore, D. M. (2009). Comparing stochastic point-source and finite-source ground-motion simulations: SMSIM and EXSIM, Bull Seismol Soc Am, Vol 99, pp 3202-3216.

Boore, D. M., Skarlatoudis, A. A., Margaris, B. N., Papazachos, C. B. and Ventouzi, C. (2009). Along-Arc and Back-Arc Attenuation, Site Response, and Source Spectrum for the Intermediate-Depth 8 January 2006 M 6.7 Kythera, Greece, Earthquake, Bull Seismol Soc Am, Vol 99, No 4, pp 2410-2434.

Boore, D. M., Stewart, J. Seyhan, E. and Atkinson, G. (2014). NGA-West2 Equations for Predicting PGA, PGV, and 5% Damped PSA for Shallow Crustal Earthquakes, Earthq Spectra, Vol 30, No 3, pp 1057-1085.

Boore D. M. and Thompson, E. M. (2014). Path Durations for Use in the Stochastic-Method Simulation of Ground Motions, Bull Seismol Soc Am, Vol 104, No 5, pp. 2541–2552.

Brune, J. N. (1970). Tectonic stress and the spectra of seismic shear waves from earthquakes, J Geophys Res, Vol 75, No 26, pp 4997-5009.

Cheng, J., Rong, Y., Magistrale, H., Chen, G. and Xu, X. (2019). Earthquake Rupture Scaling Relations for Mainland China, Seismol Res Lett, Vol 91, pp 248-261.

Crane, S. and Motazedian, D. (2014). Low-frequency scaling applied to stochastic finite-fault

Modeling, J Seismol, Vol 18, pp 109-122.

Douglas, J. (2022). Ground Motion Prediction Equations 1964-2021. Online Technique Report: http://www.gmpe.org.uk/.

Edwards, B. and Fäh, D. (2013). A Stochastic Ground-Motion Model for Switzerland, Bull Seismol Soc Am, Vol 103, No 1, pp 78-98.

Goulet, C. A., Abrahamson, N. A., Somerville, P. G. and Wooddell, K. E. (2015). The SCEC broadband platform validation exercise: Methodology for code validation in the context of seismic hazard analyses, Seismol Res Lett, Vol 86, No 1, 17–26.

Goulet, C. A., Bozorgnia, Y., Kuehn, N. Atik, L. Al, Youngs, R. R., Graves, R. W. and Atkinson, G. M. (2018). PEER 2018/08—NGA-East ground-motion models for the U.S. Geological Survey National Seismic Hazard Maps, Pacific Earthquake Engineering Research Center PEER Report 2018/08.

Hoult, R. D., Pascale, A., Jones, A., and Allen, T. (2021). The M_W 5.9 Woods Point Earthquake: A Preliminary Investigation of the Ground Motion Observations, Australian Earthquake Engineering Society, 2021 Virtual Conference, Nov. 25-26.

Katsuaki K. and T. Ohmachi (1998). Ground-Motion Characteristics Estimated from Spectral Ratio between Horizontal and Vertical Components of Microtremor, Bull Seismol Soc Am, Vol 88, No 1, pp 228-241.

Lam, N. T. K., Wilson, J. and Hutchinson, G. (2000). Generation of Synthetic Earthquake Accelerograms Using Seismological Modelling: A Review, J Earthq Eng, Vol 4, No 3, pp 321-354.

Leonard, M. (2010). Earthquake Fault Scaling: Self-Consistent Relating of Rupture Length, Width, Average Displacement, and Moment Release, Bull Seismol Soc Am, Vol 100, No 5A, pp 1971-1988.

Love, D. (2021). 2021-09-21 Woods Point Earthquake Focal Mechanism and First Arrivals, Australian Earthquake Engineering Society, 2021 Virtual Conference, Nov. 25-26.

Motazedian, D., and Atkinson, G. M. (2005). Stochastic finite-fault modeling based on a dynamic corner frequency, Bull Seismol Soc Am, Vol 95, pp 995–1010.

Jayalakshmi, S., Dhanya, J., Raghukanth, S. T. G. and Mai, P. M. (2021). Hybrid broadband ground motion simulations in the Indo-Gangetic basin for great Himalayan earthquake scenarios, Bull Earthq Eng, Vol 19, pp 3319–3348.

Katsuaki K. and T. Ohmachi (1998). Ground-Motion Characteristics Estimated from Spectral Ratio between Horizontal and Vertical Components of Microtremor, Bull Seismol Soc Am, Vol 88, No 1, pp 228-241.

Pezeshk, S., Zandieh, A., Campbell, K. W. and Tavakoli, B. (2018). Ground-Motion Prediction Equations for Central and Eastern North America Using the Hybrid Empirical Method and NGA-West2 Empirical Ground-Motion Models, Bull Seismol Soc Am, Vol 108, No 4, pp 2278-2304.

Seyhan, E. and Stewart, J. P. (2014). Semi-empirical nonlinear site amplification from NGA West2 data and simulations, Earthq Spectra, Vol 30, 1241–1256.

Sinadinovski, C., Pekevski, L. and McCue, K. (2021). Focal depth of the magnitude Mw5.9 Woods Point earthquake on 22 September 2021, from seismograms recorded on the other side of the Earth. Australian Earthquake Engineering Society, 2021 Virtual Conference, Nov. 25-26.

Somerville, P., Graves, R., Collins, N., Song, S.-G., Ni, S. and Cummins, P. (2009). Source and ground motion models for Australian earthquakes, Australian Earthquake Engineering Society 2009 Conference, Newcastle, New South Wales.

Tang, Y. (2022a). An Updated Corner-frequency Model for Stochastic Finite-fault Ground Motion Simulation, Bull Seismol Soc Am, Vol 112, No 2, pp 921-938.

Tang, Y. (2022b). GMSS2.0: An Enhanced Software Program for Stochastic Finite-fault Ground Motion Simulation, Seismol Res Letts, Vol 93, pp 1868-1879.

Tang, Y., Lam, N.T.K., Tsang, H.H. and Lumantarna, E. (2019). Use of Macroseismic Intensity Data to Validate a Regionally Adjustable Ground Motion Prediction Model, Geosciences, Vol 9, No10, pp. 1-22.

Tang, Y., Lam, N.T.K., Tsang, H.H. and Lumantarna, E. (2020). An Adaptive Ground Motion Prediction Equation for Use in Low-to-moderate Seismicity Regions, J Earthq Eng, Vol 26, No 5, pp 2567-2598.

Tang, Y., Lam, N.T.K., Tsang, H.H. (2021). A Computational Tool for Ground Motion Simulations Incorporating Regional Crustal Conditions, Seismol Res Letts, Vol 92, No 2A, pp 1129-1140.

Thingbaijam, K. K., S., Mai, P. M. and Goda, K. (2017). New Empirical Earthquake Source-Scaling Laws, Bull Seismol Soc Am, Vol 107, No 5, pp 2225-2246.

Wells, D. L. and Coppersmith, K. J. (1994). New Empirical Relationships among Magnitude, Rupture Length, Rupture Width, Rupture Area, and surface displacement, Bull Seismol Soc Am, Vol 84, No 2, pp 974-1002.